Hydrographic survey over the Carlsberg Ridge in May 2012

Hailun He[1], Yuan Wang[2], Xiqiu Han[2], Yanzhou Wei[1], Pengfei Lin[3], Zhongyan Qiu[2], and Yejian Wang[2]

[1]State Key Laboratory of Satellite Ocean Environment Dynamics, Second Institute of Oceanography, Ministry of Natural Resources, Hangzhou 310012, China
[2]Key Laboratory of Submarine Geosciences, Second Institute of Oceanography, Ministry of Natural Resources, Hangzhou 310012, China
[3]State Key Laboratory of Numerical Modeling for Atmospheric Sciences and Geophysical Fluid Dynamics, Institute of Atmospheric Physics, Chinese Academy of Sciences, Beijing 100029, China

Correspondence: Hailun He (hehailun@sio.org.cn); Xiqiu Han (xqhan@sio.org.cn)

Abstract. In May 2012, we conducted a hydrographic survey over the Carlsberg Ridge in the northwest Indian Ocean. In this paper, we use these station data, in combination with some free-floating Argo profiles, to obtain the sectional temperature and salinity fields, and subsequently, the hydrographic characteristics are comprehensively analyzed. Through the basic T-S diagram, three salty water masses, Arabian Sea High-Salinity Water, Persian Gulf Water, and Red Sea Water, are identified. The sectional data show a clear ventilation structure associated with Arabian Sea High-Salinity Water. The 35.8 psu salty water sinks at 6.9°N and extends southward to 4.4°N at depths around the thermocline, where the thermocline depth is in the range of 100 to 150 m. This salty thermocline extends much further south than the climatology indicates. Furthermore, the temperature and salinity data are used to compute the absolute geostrophic current over the specific section, and the results show meso-scale eddy vertical structure different from some widely used oceanic reanalysis data. We also find a west-propagating disturbance at 6°N, and the related features are described in terms of phase speed, horizontal and vertical structures.

1 Introduction

The northwest Indian Ocean (NWIO) is unique compared with the other two basin-scale oceans (Pacific and Atlantic Ocean) because the dominant characteristics are monsoon driven (Schott and McCreary Jr., 2001; Schott et al., 2009). The seasonal monsoon forces the coastal current back and forth and generates the renewed Somalia Current, which is always marked as the strongest current in the real ocean (as strong as 3.5 m s^{-1}). Moreover, the monsoon builds up a meridional current in the NWIO, which changing the form of the customary zonal current (as in the Pacific and Atlantic Oceans) into the meridional current. NWIO is also famous for its role in the so-called Indian Ocean Dipole (IOD; Saji et al., 1999; Webster et al., 1999; Han et al., 2014; Chen et al., 2015), which represents the zonal gradient of sea surface temperature (SST) in the Indian Ocean (IO). As a basin-wide signal, the IOD is closely related to the IO-adjacent climate (Li and Han, 2015). Some studies also emphasized the distinct meso- and submeso-scale air-sea interactions in the NWIO (Vecchi et al., 2004).

Historically, the John Murray/Mabahiss expedition (1933-1934) was an early one-time IO exploration. Later, the First International Indian Ocean Expedition (IIOE-1; 1962-1965) and the subsequent Second International Indian Ocean Expedition (IIOE-2; 2015-2020) were marked by famous international cooperation (Wooster, 1984; Aleem and Morcos, 1984; Hood et al.,

Ocean Science
Discussions

2016). Between IIOE-1 and IIOE-2, the World Ocean Circulation Experiment (WOCE, 1990-1997; Ganachaud and Wunsch, 2000, 2003) defined ten one-time sections and three repeated sections in the IO (Talley, 2013). Next, considering the importance of continuous time series data, Research Moored Array for African-Asian-Australian Monsoon Analysis and Prediction (RAMA) was implemented in the tropical Indian Ocean and delivered fixed-position environmental parameters. Also, the

5   implementation of the Array for Real-time Geostrophic Oceanography (Argo) project advanced the sampling process to be automatic and near real-time (Yin et al., 2012).

To date, the main water masses in the IO and NWIO are understood by the scientific community (Sharma et al., 1978; Kumar and Prasad, 1999; Emery, 2001; Talley et al., 2011), although some regional water masses and their short-term variations are still not well documented. The historical and present RAMA observation arrays are close to the tropic and omit the NWIO.

10 In situ observations in the NWIO mainly depend on Argo (Riser et al., 2016; Vitale et al., 2017). However, as we show later, the number of Argo floats is still too sparse to represent the meso-scale eddy field in the NWIO. The present circumstance stimulates our effort to find more observational resources.

The Carlsberg Ridge (CR) is a typical slow-spreading ridge and lies along the northwest-southeast direction in the NWIO. Recently, we conducted an interdiscipline survey on CR (Yang et al., 2016; Wang et al., 2017), and the CTD and XCTD

15 station data have not yet been explored. Hydrographic analysis of CR is necessary for at least three reasons. First, such analysis helps us to define regional ocean circulation and regional multiscale air-sea interactions. Second, the analysis supplies basic environmental parameters to determine the movements of sporadic hydrothermal activity. Third, this analysis sheds new light into the basic energy theory of ocean circulation (Huang, 1999). The trajectory of Argo float are not manually controlled; however, ship surveys could cover specified sections and have a clearer objective. Hence, this paper aims to analyze hydrographic

20 information by combining both CR expedition and Argo floats.

2   Data and methods

2.1   In situ data description

The data for our study were collected during the Chinese cruise DY125-24 (May 2012) by the Chinese research vessel "LISIGUANG". Hydrographic observations were conducted in the region of the Carlsberg Ridge. The vertical profiles of

25 temperature, conductivity and pressure were obtained by a calibrated SBE-19plus CTD and some expendable CTD (XCTD). The station information is shown in Fig. 1 and Table 1. All stations were mainly located along the CR section and therefore defined the regional along-section (y) and cross-section (x) coordinates. The maximum measurement depths of XCTD and Argo are 1050 and 2000 m, and therefore we limited our analysis to depth 2000 m. According to Talley et al. (2011) and Emery (2001), upper 2000 m depth covers the upper ocean (defined as 0-500 m) and the intermediate-depth ocean (defined as

30 500-2000 m).

Regarding data quality, an intercomparison between XCTD and CTD measurement was implemented in the southern tropical Indian Ocean. The XCTD station involved was located at 73.8ºE and 1.7ºS at 14:23 on May 4 (Coordinated Universal Time), and the counterpart CTD station was located at 73.5ºE and 1.4ºS a half-hour later (14:58 on May 4). The mean differences

Ocean Science
Discussions

in the recorded in situ temperature (salinity) were 0.425°C (0.058 psu) in the upper ocean and 0.051°C (0.053 psu) in the intermediate-depth ocean.

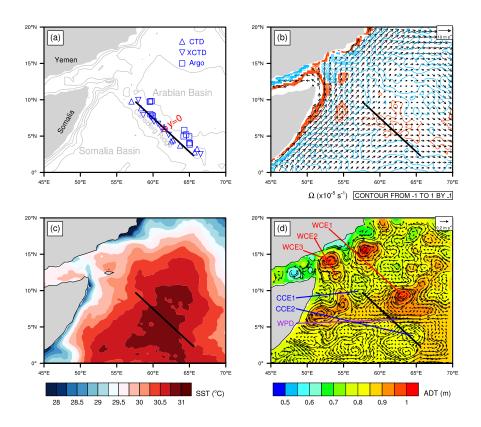**Table 1.** Information on CTD/XCTD stations and Argo floats.

Type	Station/Float	Latitude	Longitude	Time (month/day hour)
XCTD	S09CTD08	2.3°N	66.3°E	05/06 07
XCTD	S16CTD13	5.1°N	62.1°E	05/14 16
XCTD	S19CTD15	6.4°N	60.4°E	05/16 13
XCTD	S20CTD16	7.3°N	59.5°E	05/16 19
XCTD	S23CTD19	7.0°N	60.1°E	05/20 14
XCTD	S25CTD21	9.6°N	57.6°E	05/23 04
XCTD	S26CTD22	5.5°N	61.1°E	05/26 20
CTD	S10CTD09	3.1°N	66.0°E	05/07 05
CTD	S12CTD10	2.5°N	65.4°E	05/09 12
CTD	S14CTD11	4.2°N	62.3°E	05/11 17
CTD	S15CTD12	4.3°N	62.4°E	05/13 21
CTD	S17CTD14	6.2°N	61.3°E	05/15 08
CTD	S21CTD17	8.5°N	58.2°E	05/17 05
CTD	S22CTD18	9.5°N	57.0°E	05/18 07
CTD	S28CTD24	3.4°N	63.4°E	06/01 04
Argo	2901847	4.0°N	65.0°E	05/03 02
Argo	2901848	5.8°N	64.3°E	05/07 13
Argo	2900877	8.0°N	59.6°E	05/07 09
Argo	2901096	5.0°N	64.2°E	05/08 19
Argo	2901888	9.7°N	59.5°E	05/08 01
Argo	2901847	4.0°N	65.0°E	05/12 20
Argo	2901888	9.8°N	59.6°E	05/17 23
Argo	2900877	7.9°N	59.9°E	05/17 09
Argo	2901096	5.2°N	64.6°E	05/18 19
Argo	2901847	3.8°N	65.1°E	05/22 16
Argo	2900877	7.8°N	60.0°E	05/27 09
Argo	2901096	5.0°N	65.0°E	05/28 18
Argo	2901888	9.8°N	59.8°E	05/28 01

In our postprocessing, 13 simultaneous Argo profiles were found within a 200 km radius of the study region (Fig. 1 and Table 1). The Argo float is free-floating without regular calibration; therefore, quantifying the bias of Argo is relatively important

5 before using the data. Fortunately, an Argo float drifted (2900877) around an XCTD station (S20CTD16; Table 1), and the two measurements occurred on May 17 and May 16, respectively. Then, we compared the XCTD with the Argo profile, and the

Ocean Science
Discussions

Open Access

EGU

Figure 1. (a) CTD/XCTD Stations of the DY24 survey and the simultaneous Argo profiles around the CR. The CR defines local coordinates in which the x-coordinate is cross-track and the y-coordinate along-track, the corresponding origin point is selected as (61.6°E, 6.0°N), and the isobaths of -4000, -3000, -2000 and -1000 m are presented; (b) monthly mean wind vector and vorticity (Ω) from CCMP wind data, data are plotted every 3 points for wind vector, the positive and negative vorticities are displayed by red and blue contours repectively; (c) monthly mean sea surface temperature from OSTIA data; and (d) monthly mean sea surface height (absolute dynamic topography), and the consistent surface geostrophic current (shown with every 2 points) from AVISO.

mean differences in the in situ temperature (salinity) were 0.076°C (0.144 psu) in the upper ocean and 0.374°C (0.171 psu) in the intermediate-depth ocean. It is also noted that the differences for temperature and salinity in the intermediate depth ocean are much larger than those in the upper ocean, which is probably due to the oceanic internal high-wavenumber signals between two stations.

Ocean Science
Discussions

2.2 In situ data processing

All the data from several sources need to be processed to same levels because of the different sampling rates; i.e., the vertical resolutions of CTD, XCTD and Argo are 0.1, 0.1, and 2.0 m, respectively. In the first step of data postprocessing, the coarse data are moving-averaged into a uniform vertical grid with a 5 m interval starting from 5 m below the surface. Here 5 m vertical

5   resolution is sufficient for describing vertical structure of mixed-layer and water masses. Special treatment is imposed on one Argo float (2901888; three profiles; Table 1), where the coarse profiles lose data in the upper 20 m; thus, the missing data are filled with the same value as uppermost available data in the near surface.

The data are then projected into the standard CR section, with a uniform 100 km interval in the y-coordinate. We use the objective analysis method to interpolate data from irregularly spaced locations to a fixed grid (Barnes, 1994). Later, a low-pass

10   filter is imposed on the CR sectional data to remove the short-wavelength signals, which are partly from the cross-bias among different data sources and partly from the submesoscale or higher wavenumber signals in the real ocean. The low-pass filter is a two-dimensional LOcally Estimated Scatterplot Smoothing (LOESS) filter (Cleveland and Grosse, 1991), and the moving-average wavelengths are 300 km and 30 m in the horizontal and vertical directions, respectively. As a result, the smoothed data save the essential features of the thermal-salinity field but remove the noise.

15 ## 2.3 Satellite data description

2.3.1 Surface wind

We use Cross-Calibrated Multi-Platform (CCMP; Atlas et al., 2011) gridded surface vector winds here (version 2.0). CCMP data are daily products, and they are projected on 0.25°×0.25° grids.

2.3.2 Sea surface temperature

20   The sea surface temperature (SST) data is produced by Operational Sea Surface Temperature and Sea Ice Analysis (OSTIA; Donlon et al., 2011), which merges satellite infrared and microwave products, ship, buoy, etc. OSTIA is daily product, and the horizontal resolutions are 0.05°×0.05°.

2.3.3 Sea surface height

For describing the sea surface height (SSH) and the related surface geostrophic current, we use the Archiving, Validation, and

25   Interpretation of Satellite Oceanographic (AVISO) grided data. The temporal resolution is daily, and the horizontal resolutions are 0.25°×0.25°.

2.4 Reanalysis data description

As references, we also employ two widely used reanalysis datasets for comparison, aiming at evaluating the quality of reanalysis data. The first reanalysis dataset is Simple Ocean Data Assimilation (SODA, version 3.3.1; Carton and Giese, 2008; Carton

Ocean Science
Discussions

et al., 2018), whose horizontal resolutions are 0.25°×0.25° for longitude and latitude. The second reanalysis dataset is HYbrid Coordinate Ocean Model (HYCOM, version GOPS3.0:HYCOM+NCODA global 1/12° Reanalysis GLBu0.08/expt_19.1), and its horizontal resolutions are 0.08°×0.08°. Both SODA and HYCOM assimilate various in situ and satellite-based data sources: historical station profiles, Argo profiles, moorings, drifters, satellite SSTs, SSHs, etc.

2.5 Method of tracers

Using SODA reanalysis, we release some passive tracers along the CR and backtrack their trajectories based on the Lagrangian description, and the methods are formulated by

$$
\begin{cases}
X^{n-1/2} & = X^{n+1/2} - U^n \cdot \Delta t \\
Y^{n-1/2} & = Y^{n+1/2} - V^n \cdot \Delta t \\
z^{n-1/2} & = z^{n+1/2} - w^n \cdot \Delta t
\end{cases}
\tag{1}
$$

Here, X and Y are the Cartesian coordinates along longitude and latitude respectively, U and V are the corresponding currents, z is the vertical coordinate, and n is the time step. In the computation, we set the interval of time step (Δt) as 3600 s.

3 Results

3.1 Background environment

The time period of the shipboard survey start from 2012/05/06 and end at 2012/06/01 (Table 1). Figure 1(b-d) show the monthly mean surface wind, SST and SSH. In this specific month, which is preferentially defined as the later stage of monsoon transition, the summer monsoon has started but is not very strong (Fig. 1b). The along-coast wind prevails in the regional wind field, and the wind speed in the region far from the western coast is weaker. Positive wind curl along the Somalia coast and Yemen is responsible for off-coast Ekman water transport, which induces sufficient coastal upwelling to bring lower-layer cold water upward and cool the sea surface (Fig. 1c). The patterns of wind curl are roughly consistent with that of the climatological monthly mean wind stress curl (Beal et al., 2013), where the wind stress curl highlights the strong seasonal variations, particularly along the Arabian Peninsula. Otherwise, the dominant wind curl in the NWIO is negative, which is consistent with the annual mean, and denote the downwelling-preferred wind-forcing circumstance.

Wind and SST have a close relationship (Fig. 1c). The near-coast Ekman pumping generates a sharp SST front at the transition area between the coast and oceanic interior. The basin-scale semicircular SST front then outlines a warm area in the oceanic interior, where SST exceeds 30°C. The main part of the CR is located in this strikingly warm region.

On the other hand, SSH (or absolute dynamic height, ADT) shows multiple meso-scale eddies (Fig. 1d). There are some warm-core eddies (anti-cyclonic eddies), to the east of the CR (WCE1), east of the Horn of Africa (WCE2), and northeast of the Horn of Africa but very close to Yemen (WCE3). The first two warm-core eddies (WCE1 and WCE2) seem to release footprints in the wind stress curl (Fig. 1b); however, WCE3 does not induce significant wind curl anomalies. Two cold-core eddies (cyclonic eddies; CCE1 and CCE2) are also observed at either end of the CR. Besides, a remarkable westward current

is observed at the latitude of 6°N, which is noted here as a westward-propagating disturbance (WPD). WPD is pronounced compared with the circumstances around the specific region, which refers to not only the magnitude (-0.38 m/s for the zonal current) but also the zonal extent (7.5° in longitude), although its meridional extent is relatively narrow (1.3° in latitude).

3.2 Temperature, salinity and density

5   First, we impose the water mass analysis on the objective-analysis data (section 2.2), and the results are shown in Fig. 2. The data support that the upper water is more saline than the Indian Equatorial Water (IEW) and fresher than the Arabian Sea Water (ASW). The observed waters are likely to be mixed IEW and ASW. When the latitude spans from the tropical band (2.3-5°N in the present study) to the subtropical band (5-9.7°N in the present study), the salinity generally increases, consistent with the northern-side ASW being much more saline than the southern-side IEW (Han et al., 2014) and this meridional variation

10   in salinity is due to the different proportions of IEW and ASW. On the northwest side, water columns contain Arabian Sea High-Salinity Water (ASHSW), which are observed as saline water at a potential density of approximately 24 kg/m^3 (Kumar and Prasad, 1999).

The intermediate waters (500 - 1500 m) from our data are projected as Persian Gulf Water (PGW, Prasad et al., 2001) and Red Sea Water (RSW, Beal et al., 2000; Talley et al., 2011). According to Kumar and Prasad (1999), the definition of PGW

15   (RSW) is the density range as 26.2-26.8 kg/m^3 (27.0-27.4 kg/m^3), temperature range 13-19°C (9-11°C), and the salinity range 35.1-37.9 psu (35.1-35.7 psu). Despite RSW is deeper than PGW, both PGW and RSW are defined as Red Sea-Persian Gulf intermediate water (RSPGIW; Emery, 2001).

Sectional snapshots of temperature and salinity are shown in Fig. 3. The thermocline is in the depth range of 100 to 150 m (20°C isothermal line, Xie et al., 2002). From the present snapshot, the thermocline is nearly flat at the tropical band and

20   deepens northward in the subtropical band. This phenomenon is also supported by the climatological data, which reveal that the sectional distribution of the thermocline is similar to a long-standing geostrophic balanced signal. In the near surface, some isothermal lines rise to the surface on the northern side and show a clear ventilation structure such that subsurface water can take part in the air-sea interaction. Meanwhile, for the intermediate water, the isothermal line tilts deeper from south to north.

The striking feature of the salinity field is that a salinity tongue appears at 100 m depth, where the salty water is ASHSW

25   (Kumar and Prasad, 1999). Climatological data show that these salty waters originate from the north side and extend southward; however, in our survey, the extent is greater. We emphasize the iso-salinity line of 35.8 psu; the southern extension can reach y=150 km (or 6.9°N) in climatology but -250 km (or 4.4°N) in our survey. This result means that the salty water extends southward more than 2.5° in latitude in excess of climatology. The present observation also shows the salty intermediate water as PGW and RSW. The observation shows slightly more saline water than climatology on the northern side, although the

30   overall structure is mostly consistent with the climatology.

When we move forward to the potential density field, the appearance of the 22 kg/m^3 isopycnal is evident in both the snapshot and climatology. For the snapshot, the outcrop point of the 22 kg/m^3 isopycnal is y=300 km, or 7.8°N. It is worth noting that the outcrop point is near the transition point for signs of wind vorticity when we project the outcrop point in the
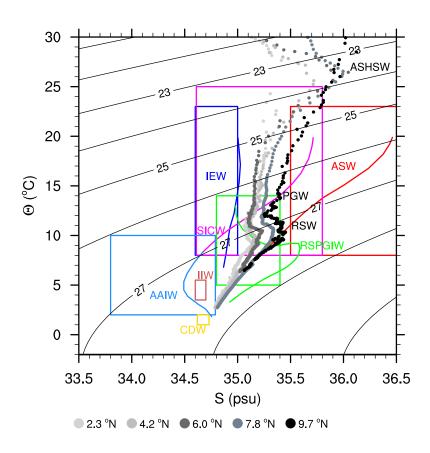
Figure 2. T-S diagram for the upper 1050 m of water on the CR. The water masses are defined in Emery (2001) and include the Arabian Sea water (ASW), Indian equatorial water (IEW), South Indian central water (SICW), Antarctic intermediate water (AAIW), Indonesian intermediate water (IIW), Red Sea-Persian Gulf intermediate water (RSPGIW), and circumpolar deep water (CDW). The color lines are the mean T-S curves (Figure 8 in Emery (2001)), and the rectangles represent the appropriate temperature and salinity ranges (Table 1 in Emery (2001)). In addition, Red Sea water (RSW), Persian Gulf water (PGW), and Arabian Sea High-Salinity Water (ASHSW) are also represented in the present analysis.

wind vector field (Fig. 1b). The north side of the outcrop point has negative wind vorticity, which promotes downwelling. Ventilation is highly related to the downwelling of high-salinity water and its southern extension (Luyten et al., 1983).

Fig. 3 also shows the reanalysis data, and essentially, the reanalysis captures the thermal structure quite well compared with the present observations and climatology. For instance, in the upper ocean, the surface warm water is distributed on the

south side and northward to y=400 km where it crops out. The observed sharply descending thermocline near y=100 km is reproduced in SODA and HYCOM. It is also noted that the tropical near-surface upwelling in HYCOM has some evidence from the present observations. For the intermediate-depth water, in SODA and HYCOM, the isothermal lines also tilt deeper from south to north, which resembles both the present observations and the climatology.

5   For salinity, the remarkable southward extension of salty water in the upper ocean is also captured by SODA and HYCOM, and the southward extension in HYCOM approaches the observations more closely. In the intermediate-depth water, the southward extension from the north side in SODA is similar to the observations, while the corresponding signal in HYCOM is obscured.

The upper ocean density fields from SODA and HYCOM also show clear ventilation structures. From the observations, tropical waters with a potential density of 22 kg/m^3 at a depth of 30 m are rising to the surface. The outcrop points of a potential density of 22 kg/m^3 in SODA and HYCOM are shifted southward compared with the observations. Additionally, the near-surface upwelling in the tropical band in HYCOM is strong, but not significant in the observations.

3.3 Cross-track current

The geostrophic current is deduced from the in situ density field by thermal wind theory (Fig. 4), where the velocity is integrated downward from the surface geostrophic current (Lagerloef et al., 1999). The velocity field is remarkable in the upper ocean, where the current field is dominated by meso-scale eddies. The cross-track current in the tropical band is induced by CCE2. The structure of CCE2 is asymmetric, and the positive cross-track flow is stronger than the negative counterpart. In contrast, the subtropical band is identified as the margin of a warm-core eddy, which is located northwest of the CR. At 6°N latitude, the vertical structure of WPD is well rebuilt in Fig. 4a. WPD seems to extend vertically to a depth of 200 m, and the horizontal extent is near 200 km for the current greater than 0.02 m/s. Meanwhile, the maximum cross-track current of the disturbance is 0.12 m/s. Furthermore, Fig. 5 is the Hovmöller plot of the surface zonal current at 6°N latitude (surface geostrophic current from SSH). The WPD are observed to start at 69°E on day 102, propagate westward with a phase speed of 0.2 m s^{-1} and arrive at 60°E on day 155. The current field also captures the northeast current (less than 0.075 m/s) in the intermediate depth (-200 $\leq y \leq$ -20 km, and 150 $\leq y \leq$ 350 km), which is due to the corresponding isothermal tilting (Fig. 3).

25   For the reanalysis data, as shown in Fig. 4, although the surface currents are similar due to the assimilation of SSH in the reanalysis process, the cross-track current from reanalysis is quite different from the observation-based absolute geostrophic current. The differences are observed in three aspects. First, the meso-scale eddy CCE2 is not well represented for the vertical structure, as SODA and HYCOM limit the southern part of CCE2 to the upper 200 m, when the current speed is faster than 0.05 m/s. Meanwhile, in SODA and HYCOM, the northern part of the meso-scale eddy (CCE2) has much latitude expansion, and merges the disturbance (WPD). Second, the undercurrent in the southern portion of the observations differs from those in SODA and HYCOM. The undercurrent in SODA is relatively weak, while HYCOM shows a northward shift of the current core. Finally, for the northern portion, SODA gives a relatively shallow depth for the surface northeast current, and the corresponding horizontal extent exceeds that of the observations. The locations of surface zero current in SODA and observation are y=170 and 240 km, respectively.

Ocean Science
Discussions

3.4 Tracers

Where the pathways of ASHSW and RSW are concerned, the explanations are still ambiguous. ASHSW and RSW are formed near the northern side of the NWIO; therefore, according to the customary ocean ventilation theory, ASHSW and RSW sink and move southward along the isopycnal layer from the generation zone following the wind-driven current (Luyten et al., 1983).

5 However, the feasibility of the ocean ventilation theory is still under debate, especially for the northern IO, whose meridional extent is limited compared with the other two basins. For instance, in situ potential vorticity analysis on RSW reveals that the flows generally follow the zonal direction (Beal et al., 2000). Here, the SODA reanalysis supplies compact datasets for passive tracers; therefore, we set some passive tracers along the CR and backtrack their trajectories using the Lagrangian description (section 2.5), and the results are shown in Fig. 6.

10 For the ASHSW, we set the tracers at a depth of 100 m, and the trajectories reveal different pathways on the CR. For the tropical band (Fig. 6e), the water mainly follows the zonal movement, but the near-equator tracers are from west side and relatively north-side tracers come from east side. While for latitudes from 5-8°N (Fig. 6c), the water mainly originates from the northeast side, and the trajectories resemble those of the ventilation theory. For latitudes from 8-9.8°N (Fig. 6a), the trajectories look like the flow of the summer Somalia Current (Schott et al., 2009).

15 For the RSW in the intermediate-depth layer at 700 m, the trajectories in the tropical band (Fig. 6f) and at latitudes from 5-8°N (Fig. 6d) generally follow the zonal movement (Beal et al., 2000). The tracer movements at latitudes from 8-9.8°N (Fig. 6b) partly agree with those of the ventilation theory, and partly follow the zonal direction (Beal et al., 2000).

4 Discussion

The CTD and XCTD data are precise in reconstructing the three-dimensional oceanic data. The Argo-only data are not sufficient

20 to describe the meso-scale eddy in the NWIO. In the present study, the maximum distance between Argo profiles is 500 km along the CR; however, after adding the shipboard station data, the maximum distance decreases to 100 km, which falls into the eddy-permitting scale. Sufficient sampling produces more reliable vertical structures of temperature, salinity and density.

The most remarkable signal in the upper ocean is the southward extension of ASHSW, where the counterpart in the climatology data exists but is weak in the horizontal extension. It is surprising that the HYCOM reanalysis captures the phenomenon

25 well, while SODA shows some disadvantages. We speculate that although both SODA and HYCOM assimilate the Argo data into an Oceainc General Circulation Model (OGCM), the methodology of assimilation or the weight between OGCM and in situ observations, is sharply different. We assume the southward extension of ASHSW could be simulated by the dynamic core of OGCM, and the phenomenon was not captured in the Argo-only observation, therefore, HYCOM seems more to approach the dynamic model, and SODA weighted more on the Argo-only observations. Additionally, the finer horizontal resolution

30 of HYCOM likely helps HYCOM involve more physically sound mechanics, such as the downwelling of salty water and wind-driven meridional movement.

Although the geostrophic balance is not universally suitable, it represents a good approximation to the real ocean; therefore, under the circumstance without in situ current observations, the deduced absolute geostrophic current gives alternative results

for the ocean current. In the comparative analysis, the state-of-the-art reanalysis is still insufficient to provide good current data. Although similar sea surface dynamic heights are taken into account, the incorrect density field leads to a false baroclinic mode. It is also noted that the bias is probably further amplified in OGCM and leads to potential unrealistic simulations if these reanalysis data are used in the model for initialization and boundary forcing.

5 Conclusions

This paper reports a onetime hydrographic survey on the CR in the NWIO, where the latitudes cover the tropical (2.3-5°N) and subtropical (5-9.6°N) bands. The station CTD/XCTD sampling plus the Argo floats build the sectional structures of temperature and salinity as well as density. The striking feature is the southern extension of ASHSW from northwest of the CR in the upper ocean. Meanwhile, the temperature and density fields display clear ventilation structures. In the intermediate depth, the observations also capture the RSW at a depth near 700 m.

Furthermore, we integrate the density field to obtain the absolute geostrophic current. The vertical structure of the cross-track current reveals strong signals of meso-scale eddies in the upper ocean and relatively weak northeastward current in the intermediate depth. We also identify a strong westward-propagating disturbance at a latitude of 6°N. The longitude and latitude lengths are 7.5° and 1.3° respectively. The corresponding phase speed is 0.2 m/s, and the vertically affected depth is roughly 200 m.

We further evaluate the state-of-the-art reanalysis with the present observations. As a result, because the Argo profiles and satellite SSH are assimilated into the reanalysis datasets, HYCOM and SODA show relatively good qualities for temperature, salinity and density. However, the reanalysis cross-track currents show large discrepancies compared with the absolute geostrophic current. Most importantly, HYCOM and SODA misinterpret some meso-scale eddies in the current field.

The present analysis shows potential data applications for the future, where the meso-scale eddies are relatively important but cannot be well described by the Argo-only data source. The present situation of insufficient sampling prompts more research activity in the NWIO.

Competing interests. The authors declare that they have no conflict of interest.

Ocean Science
Discussions

References

Aleem, A. A. and Morcos, S. A.: John Murray/Mabahiss expedition versus the International Indian Ocean Expedition (IIOE) in retrospect, Deep Sea Research Part A. Oceanographic Research Papers, 31, 583–588, 1984.

Atlas, R., Hoffman, R. N., Ardizzone, J., Leidner, S. M., Jusem, J. C., Smith, D. K., and Gombos, D.: A cross-calibrated, multiplatform
5   ocean surface wind velocity product for meteorological and oceanographic applications, Bull. Amer. Meteor. Soc., 92, 157–174, 2011.

Barnes, S. L.: Applications of the Barnes Objective Analysis Scheme. Part I: Effects of Undersampling, Wave Position, and Station Randomness, J. Atmos. Oceanic Technol., 11, 1433–1448, 1994.

Beal, L. M., Ffield, A., and Gordon, A. L.: Spreading of Rea Sea overflow waters in the Indian Ocean, J. Geophys. Res., 105, 8549–8564, 2000.

10 Beal, L. M., Hormann, V., Lumpkin, R., and Foltz, G.: The Response of the Surface Circulation of the Arabian Sea to Monsoonal Forcing, J. Phys. Oceanogr., 43, 2008–2022, 2013.

Carton, J. A. and Giese, B. S.: A reanalysis of ocean climate using Simple Ocean Data Assimilation (SODA), Monthly Weather Review, 136, 2999–3017, 2008.

Carton, J. A., Chepurin, G. A., and Chen, L. G.: SODA3: A new ocean climate reanalysis, J. Clim., 31, 6967–6983, 2018.

15 Chen, G. X., Han, W. Q., Li, Y. L., Wang, D. X., and J., M. M.: Seasonal-to-interannual time scale dynamics of the equatorial undercurrent in the Indian Ocean, J. Phys. Oceanogr., 54, 1532–1553, 2015.

Cleveland, W. S. and Grosse, E.: Computational methods for local regression, Stat. Comput., 1, 47–62, 1991.

Donlon, C. J., Martin, M., Stark, J. D., Roberts-Jones, J., E., F., and W., W.: The Operational Sea Surface Temperature and Sea Ice analysis (OSTIA), Remote Sensing of the Environment, 116, 140–158, 2011.

20 Emery, W. J.: Water Types and Water Masses*, in: Encyclopedia of Ocean Sciences (Second Edition), edited by Steele, J. H., pp. 291 – 299, Academic Press, Oxford, second edition edn., https://doi.org/https://doi.org/10.1016/B978-012374473-9.00108-9, 2001.

Ganachaud, A. and Wunsch, C.: Improved estimates of global ocean circulation, heat transport and mixing from hydrographic data, Nature, 408, 453–457, 2000.

Ganachaud, A. and Wunsch, C.: Large-scale ocean heat and freshwater transports during the World Ocean Circulation Experiment, J. Clim.,
25 16, 696–705, 2003.

Han, W. Q., Vialard, J., McPhaden, M. J., Lee, T., Masumoto, Y., Feng, M., and DE Ruijter, W. P. M.: Indian Ocean decadal variability: A review, Bulletin of the American Meteorological Society, 95, 1679–1703, 2014.

Hood, R. R., Urban, E. R., McPhaden, M. J., Su, D., and Raes, E.: The 2nd International Indian Ocean Expedition (IIOE-2): Motivating new exploration in a poorly understood basin, Association for the Sciences of Limnology and Oceanography, 25, 117–124, 2016.

30 Huang, R. X.: Mixing and energetics of the oceanic thermohaline circulation, J. Phys. Oceanogr., 29, 727–746, 1999.

Kumar, S. P. and Prasad, T. G.: Formation and spreading of Arabian Sea high-salinity water mass, J. Geophys. Res. Oceans, 104, 1455–1464, 1999.

Lagerloef, G. S. E., Mitchum, G. T., Lukas, R. B., and Niiler, P. P.: Tropical Pacific near-surface currents estimated from altimeter, wind, and drifter data, J. Geophys. Res.-Oceans, 104, 23 313–23 326, 1999.

35 Li, Y. L. and Han, W. Q.: Decadal sea level variations in the Indian Ocean investigated with HYCOM: Roles of climate modes, ocean internal variability, and stochastic wind forcing, J. Clim., 28, 9143–9165, 2015.

Luyten, J. L., Pedlosky, J., and Stommel, H. M.: The ventilated thermocline, J. Phys. Oceanogr., 13, 292–309, 1983.

Prasad, T. G., Ikeda, M., and Kumar, S. P.: Seasonal spreading of the Persian Gulf Water mass in the Arabian Sea, J. Geophys. Res. Oceans, 106, 17 059–17 071, 2001.

Riser, S. C., Freeland, H. J., Roemmich, D., Wijffels, S., Troisi, A., Belbeoch, M., Gilbert, D., Xu, J., Pouliquen, S., Thresher, A., Le Traon, P.-Y., Maze, G., Klein, B., Ravichandran, M., Grant, F., Poulain, P.-M., Suga, T., Lim, B., Sterl, A., Sutton, P., Mork, K.-A., Velez-Belchi,

5   P. J., Ansorge, I., King, B., Turton, J., Baringer, M., and Jayne, S. R.: Fifteen years of ocean observations with the global Argo array, Nature Climate Change, 6, 145–153, 2016.

Saji, N. H., Goswami, B. N., Vinayachandran, P. N., and Yamagata, T.: A dipole mode in the tropical Indian Ocean, Nature, 401, 360–363, 1999.

Schott, F. A. and McCreary Jr., J. P.: The monsoon circulation of the Indian Ocean, Progress in Oceanography, 51, 1–123, 2001.

10   Schott, F. A., Xie, S. P., and McCreary Jr., J. P.: Indian Ocean circulation and climate variability, Reviews of Geophysics, 47, RG1002, 2009.

Sharma, G. S., Gouveia, A. D., and Satyendranath, S.: Incursion of the Pacific Ocean water into the Indian Ocean, Proc. Indian Acad. Sci., 87A, 29–45, 1978.

Talley, L. D.: Hydrographic Atlas of the World Ocean Circulation Experiment (WOCE). Volume 4: Indian Ocean, 2013.

Talley, L. D., Pickard, G. L., Emery, W. J., and S., J. H.: Descriptive physical oceanography: An introduction, Elsevier, Burlingham, 6 edn.,

15   2011.

Vecchi, G. A., Xie, S. P., and Fischer, A. S.: Ocean-atmosphere covariability in the Western Arabian Sea, Journal of Climate, 17, 1213–1224, 2004.

Vitale, S. S., DiMarco, S. F., Seidel, H. F., and Wang, Z. K.: Circulation analysis in the northwest Indian Ocean using ARGO floats and surface drifter observations, and SODA reanalysis output, Dynamics of Atmospheres and Oceans, 78, 57–70, 2017.

20   Wang, Y. J., Han, X. Q., Petersen, S., Frische, M., Qiu, Z. Y., Li, H. M., Li, H. L., Wu, Z. C., and Cui, R. Y.: Mineralogy and trace element geochemistry of sulfide minerals from the Wocan Hydrothermal Field on the slow-spreading Carlsberg Ridge Indian Ocean, Ore Geology Reviews, 84, 1–19, 2017.

Webster, P. J., Moore, A. M., Loschnigg, J. P., and Leben, R. R.: Coupled ocean-atmosphere dynamics in the Indian Ocean during 1997-98, Nature, 401, 356–360, 1999.

25   Wooster, W. S.: International studies of the Indian Ocean, 1959-1965, Deep Sea Research Part A. Oceanographic Research Papers, 31, 589–597, 1984.

Xie, S. P., Annamalai, H., Schott, F. A., and McCreary Jr., J. P.: Structure and mechanisms of south Indian Ocean climate variability, J Clim, 15, 864–878, 2002.

Yang, G., He, H. L., Wang, Y., Han, X. Q., and Wang, Y. J.: Evaluating a satellite-based sea surface temperature by shipboard survey in the

30   Northwest Indian Ocean, Acta Oceanologica Sinica, 35, 52–58, 2016.

Yin, X. Q., Qiao, F. L., Yang, Y. Z., Xia, C. S., and Chen, X. Y.: Argo data assimilation in ocean general circulation model of Northwest Pacific Ocean, Ocean Dynamics, 62, 1059–1071, 2012.
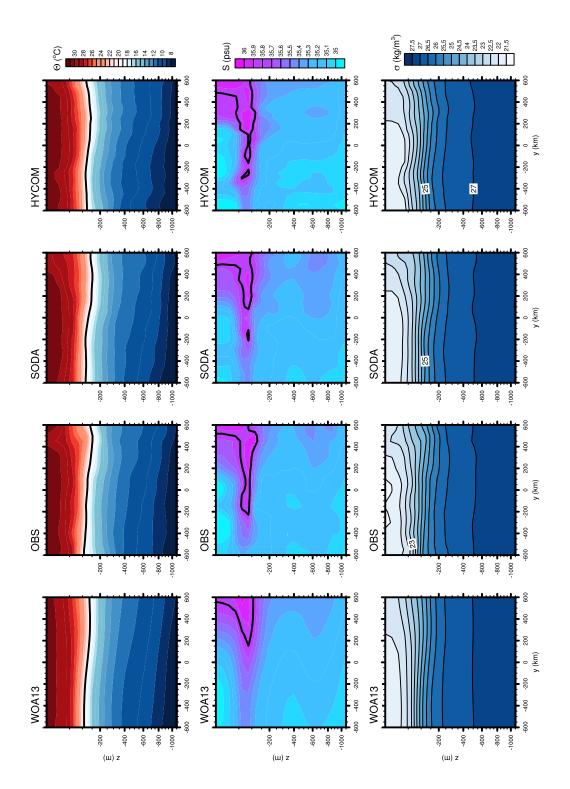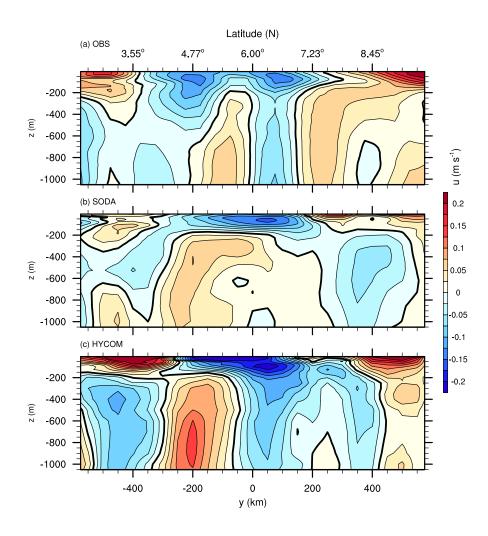
Figure 3. Sectional profiles of potential temperature (upper panels), salinity (middle panels) and potential density (lower panels). The data sources cover the WOA climatology (WOA13, version 2.0/A5B2), the present observations, and two reanalysis datasets, SODA and HYCOM. The isothermal lines of 20°C are presented at potential temperatures, and the iso-salinity lines of 35.8 psu are highlighted in the salinity fields.
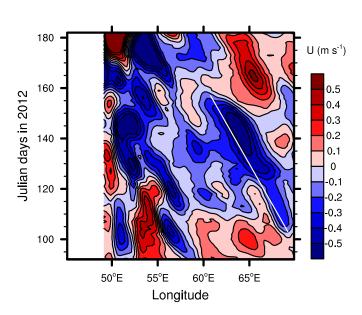
Figure 4. Sectional cross-track current: (a) absolute geostrophic current; (b and c) currents in SODA and HYCOM reanalysis, respectively. Northeastward current is positive. Thick black lines are the zero contours.
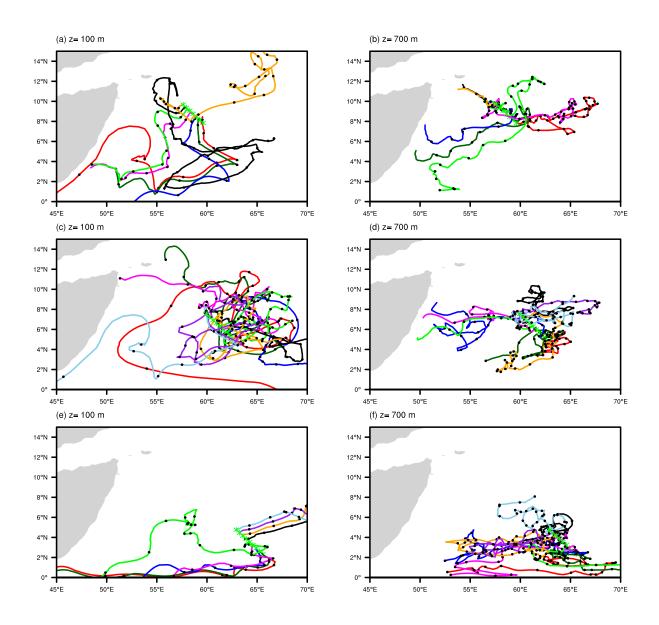
Figure 5. Hovmöller plot of surface zonal current (U) along 6°N latitude (surface geostrophic current from SSH). The white line denotes that the phase speed of the westward-propagating signal is approximately 0.2 m/s.

16

Figure 6. Passive tracers using SODA reanalysis. The tracers are set along the CR on May 15, 2012 (denoted by green asterisks), and then backward integrated to Jan. 1, 2010. The time interval is one month, as denoted by the black dots. (a-b) 8-9.8°N; (c-d) 5-8°N; (e-f) 2-5°N.